

Decomposing Large-Scale Ising Problems on FPGAs: A Hybrid Hardware Approach

Ruihong Yin, Yue Zheng, Chaohui Li, Ahmet Efe, Abhimanyu Kumar, Ziqing Zeng, Ulya R. Karpuzcu, Sachin S. Sapatnekar, and Chris H. Kim

University of Minnesota

{yin00473, zhen0631, li003135, efe00002, kumar663, zeng0083, ukarpuzc, sachin, chriskim}@umn.edu

Abstract

Emerging analog computing substrates, such as oscillator-based Ising machines, offer rapid convergence times for combinatorial optimization but often suffer from limited scalability due to physical implementation constraints. To tackle real-world problems involving thousands of variables, problem decomposition is required; however, performing this step on standard CPUs introduces significant latency, preventing the high-speed solver from operating at full capacity. This work presents a heterogeneous system that offloads the decomposition workload to an FPGA, tightly integrated with a custom 28nm Ising solver. By migrating the decomposition logic to reconfigurable hardware and utilizing parallel processing elements, the system minimizes the communication latency typically associated with host-device interactions. Our evaluation demonstrates that this co-design approach effectively bridges the speed gap between digital preprocessing and analog solving, achieving nearly 2 \times speedup and an energy efficiency improvement of over two orders of magnitude compared to optimized software baselines running on modern CPUs.

1 Introduction

Combinatorial optimization problems (COPs), including Boolean Satisfiability (SAT), MaxCut, graph partitioning, and scheduling, are widely used in circuit design, logistics, machine learning, and many other domains. However, these NP-hard problems present substantial computational challenges at scale on conventional von Neumann architectures. The exponential growth of solution space with problem size has motivated the exploration of alternative computing paradigms that exploit physical dynamics to accelerate optimization.

1.1 Ising Machines for Combinatorial Optimization

Many COPs can be naturally formulated as Ising models [1], minimizing an energy function (Hamiltonian):

$$H(\mathbf{s}) = - \sum_{i=1}^N \sum_{j=1}^N J_{ij} s_i s_j - \sum_{i=1}^N h_i s_i, \quad (1)$$

where $s_i \in \{-1, +1\}$ represents spin variables, h_i are local field terms, and J_{ij} encode pairwise couplings. This formulation represents the problem as a fully connected graph where nodes represent

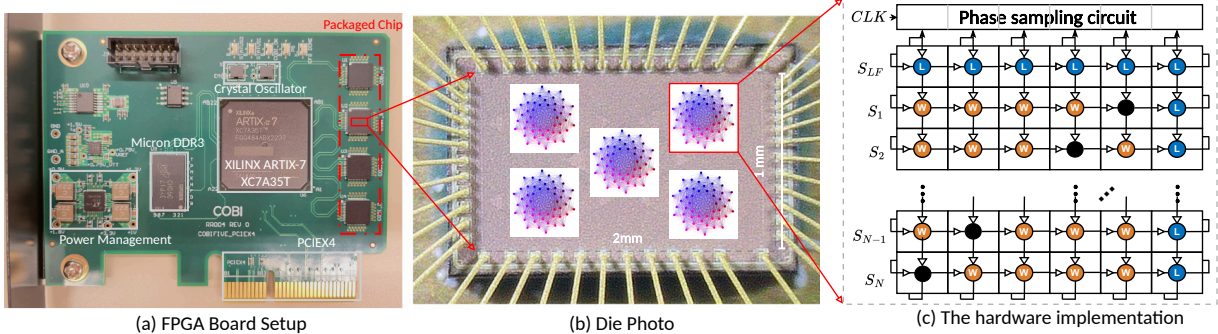


Figure 1: (a) FPGA setup showing the FPGA decomposition accelerator (Xilinx Artix-7 XC7A35T) integrated on the same board with the Ising core. This on-board co-location eliminates PCIe communication overhead and enables microsecond-scale subproblem transfer. (b) Die photograph showing five COBI chips, each supporting 50 fully-connected spins. (c) Hardware implementation: an all-to-all array of CMOS ring oscillators (ROs) designed to solve the Ising problem.

spins and edges encode coupling strengths. Physical Ising machines settle to low-energy ground states, providing solutions to the mapped problems [2].

Various Ising hardware accelerators have been proposed: quantum annealers using superconducting qubits [3], coherent Ising machines using optical parametric oscillators [4], and CMOS-based implementations using coupled ring oscillators [5, 6]. Among these, CMOS ring-oscillator (RO) based systems offer practical advantages: room-temperature operation, mature manufacturing technology, and microsecond-scale convergence with milliwatt power consumption. These systems exploit injection locking synchronization, where coupled oscillators naturally evolve to phase configurations that minimize the Ising Hamiltonian. Figure 1c shows the hardware implementation: an all-to-all array of CMOS ring oscillators where each RO represents one spin variable.

1.2 The Coupled Oscillator Based Ising (COBI) Chip: A 50-Spin RO-Based Ising Solver

Our work builds upon a 28nm CMOS Ising chip featuring 50 coupled ring oscillators with all-to-all connectivity. The chip achieves convergence within $77.5 \mu\text{s}$ per subproblem with power consumption under 10 mW, orders of magnitude faster than software solvers. Figure 1 shows the fabricated hybrid system with the FPGA decomposer (Xilinx Artix-7 XC7A35T) and COBI chip integrated on the same board. However, this μs -scale execution speed creates a system-level challenge: decomposition logic feeding subproblems becomes the critical bottleneck.

1.3 The Scalability Challenge: Decomposition is Essential

Physical constraints limit the COBI chip to 50 spins, while real-world problem instances often require thousands of variables. When problem size N exceeds hardware capacity $C = 50$, decomposition becomes necessary [7]. The global optimization problem must be partitioned into a sequence of hardware-sized subproblems, each solved iteratively on the COBI chip. This decomposition pipeline involves: (1) graph traversal to identify strongly coupled variable clusters, (2) Subproblem Generation (SubQ) with boundary clamping, (3) hardware solving on the COBI chip, and (4) global state updates. This process repeats until convergence.

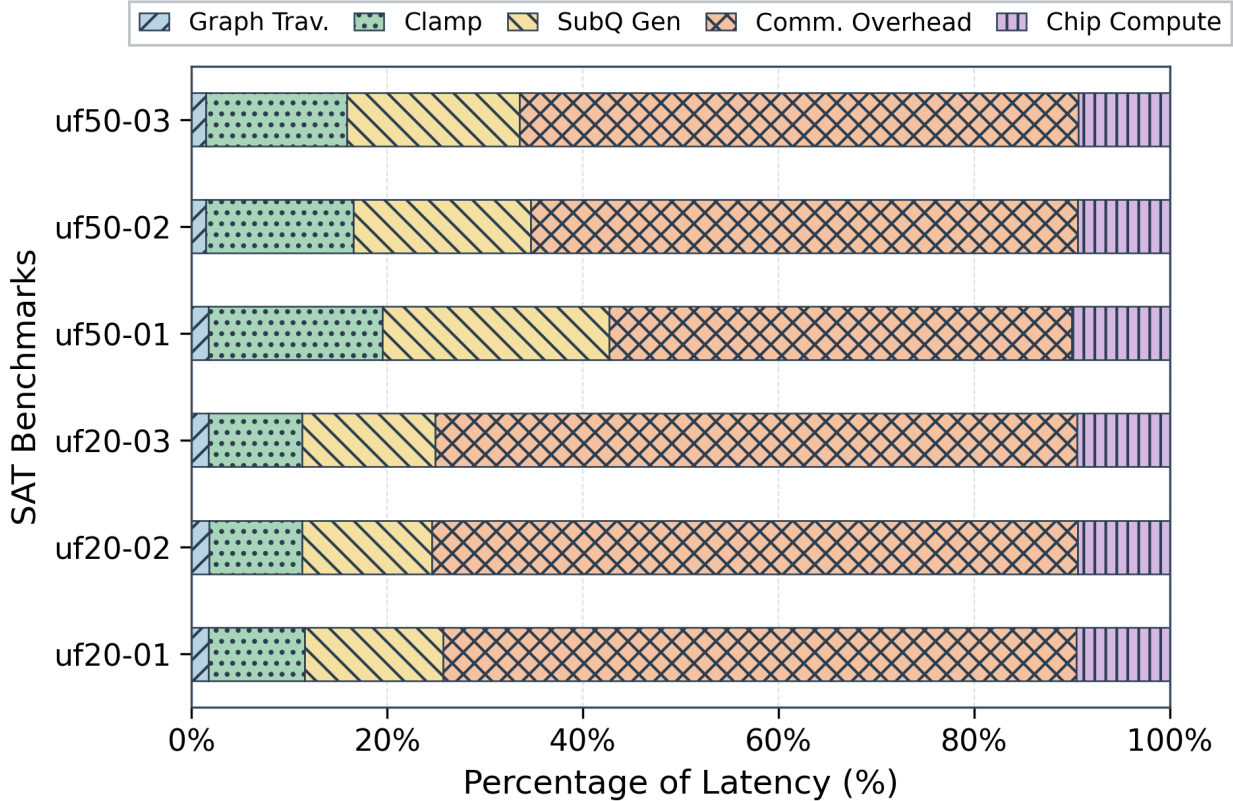


Figure 2: Communication overhead analysis for CPU-based decomposition. PCIe data transfer latency dominates the decomposition pipeline, creating a bottleneck that prevents efficient utilization of the fast COBI Ising solver. This motivates co-locating decomposition logic with the Ising core using lightweight interfaces.

1.4 The Decomposition Bottleneck

Existing decomposition frameworks run on host CPUs, treating the Ising chip as an external accelerator accessed via Peripheral Component Interconnect Express (PCIe). This arrangement creates a critical temporal mismatch: the COBI chip operates at μs time scales while CPU-based decomposition incurs millisecond-scale overhead due to sequential memory access, cache misses during irregular graph traversal, and PCIe communication latency. Our profiling reveals that the Ising accelerator remains idle over 84.9% of the time, awaiting the next subproblem (Figure 2). Figure 3 shows that PCIe data transfer accounts for approximately 62% of iteration latency in the baseline system.

1.5 Our Approach: FPGA-Accelerated Decomposition

We present a hybrid hardware architecture that co-locates an FPGA-based decomposer with the COBI chip. By integrating the FPGA on the same board with lightweight serial interfaces, we reduce subproblem transfer latency by $2.66\times$ compared to PCIe (averaging $120.5\ \mu\text{s}$ vs. $321.57\ \mu\text{s}$). The FPGA decomposer exploits dual-level parallelism (spatial parallelism via P parallel processing elements and task-level pipelining) combined with Compressed Sparse Row (CSR)-based streaming memory access. Our 100 MHz FPGA implementation achieves $1.93\times$ geomean speedup and over $150\times$ energy reduction versus an optimized C++ baseline on a modern host CPU.

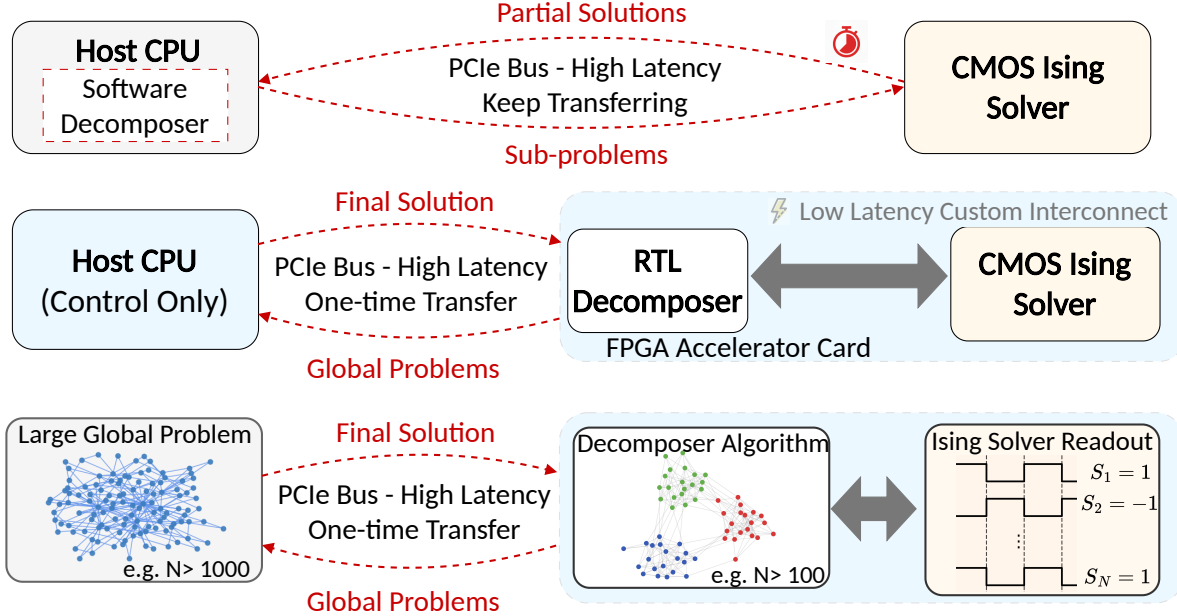


Figure 3: Architectural comparison between the conventional software-based decomposition approach and the proposed FPGA-accelerated framework. (Top) The baseline system suffers from high-latency iterative data transfers over the PCIe bus. (Middle) The proposed architecture offloads the decomposition logic to RTL, enabling a one-time global problem transfer and low-latency local interconnects. (Bottom) The corresponding algorithmic data flow illustrating the transformation from the large-scale global problem ($N > 1000$) to local sub-problems.

1.6 Contributions

- **Hybrid FPGA-Ising Architecture:** We present an FPGA decomposer (Xilinx Artix-7) tightly coupled with a 28nm 50-spin Ising chip through on-board integration, featuring micro-architectural datapath design, memory subsystem organization, and custom communication interfaces.
- **Dual-Level Parallelism:** We introduce spatial parallelism via P parallel processing elements and task-level pipelining that overlaps graph traversal with Ising solving, combined with CSR-based streaming memory access to mitigate irregular memory access patterns.
- **Hardware Validation:** Experimental evaluation on 3SAT benchmarks demonstrates 1.93× geometric speedup and over 150× energy reduction versus optimized CPU software, validating the efficacy of system-level co-design for Ising-based acceleration.

2 Background and Related Work

2.1 SAT, QUBO, and Ising Formulation

The Boolean Satisfiability (SAT) problem asks whether there exists an assignment of Boolean variables that satisfies all clauses in a given formula. As the first proven NP-complete problem, SAT serves as a canonical benchmark for combinatorial optimization [1]. The 3SAT variant, where each clause contains exactly three literals, is particularly significant: Cook’s theorem shows that any

NP problem can be efficiently reduced to 3SAT [1], making it a versatile abstraction for diverse optimization problems from scheduling, planning, circuit verification, and graph coloring.

3SAT problems are mapped to Quadratic Unconstrained Binary Optimization (QUBO) through the Chancellor construction [8], then transformed to the Ising Hamiltonian via variable substitution $s_i = 2x_i - 1$, yielding:

$$H(\mathbf{s}) = - \sum_{i=1}^N \sum_{j=1}^N J_{ij} s_i s_j - \sum_{i=1}^N h_i s_i, \quad (2)$$

where $s_i \in \{-1, +1\}$ are spin variables, h_i are local field coefficients, and J_{ij} represent pairwise spin couplings [2, 1]. While 1-SAT and 2-SAT clauses map directly to quadratic terms, 3-SAT clauses require auxiliary spins to maintain quadratic structure [8]. The choice of encoding affects both problem size and coupling density, important factors for hardware implementation. When problem size N exceeds hardware capacity C (typically $C \leq 50$ for all-to-all systems), decomposition becomes necessary to partition the global problem into hardware-sized subproblems [7].

2.2 Decomposition Strategies

Decomposition partitions large optimization problems into hardware-sized subproblems that are solved iteratively [7]. D-Wave’s qbsolv [7] and energy-impact-based methods [9] provide general-purpose decomposition strategies, while hybrid classical-quantum approaches [10] and multilevel coarsening techniques [11] trade preprocessing time for solution quality. For 3SAT problems on all-to-all connected hardware, graph-based decomposition methods such as Breadth-First Search (BFS) exploit the locality principle that strongly coupled variables (neighbors in the Quadratic Unconstrained Binary Optimization (QUBO) graph) should be optimized together to preserve clause structure and accelerate convergence [12, 13].

2.3 Hardware Implementations for Ising Machines

Digital solvers offer precision and flexible connectivity via discrete emulation but suffer from high latency and energy costs due to the von Neumann bottleneck, especially for large dense problems [14, 15, 16]. Conversely, analog implementations leverage device physics for rapid, low-power convergence [3, 17, 6, 4]. However, they are fundamentally limited by device noise and sparse connectivity, preventing the direct mapping of large-scale, fully-connected instances.

This work addresses both challenges through a hybrid FPGA-analog architecture. By co-locating FPGA-based decomposition logic with analog COBI chips, we eliminate the von Neumann bottleneck for decomposition operations while exploiting analog efficiency for the core Ising solver. The FPGA handles graph partitioning, clamping, and subproblem generation with spatial parallelism, bridging the connectivity gap between large problem instances and the analog hardware’s limited capacity. This approach combines the precision and scalability of digital decomposition with the speed and energy efficiency of analog computation, enabling practical deployment on problems far exceeding hardware constraints.

3 Problem Formulation and Decomposition Flow

This section presents our approach for solving large 3SAT instances on capacity-constrained Ising machines. We employ the Chancellor construction [8] for mapping 3SAT to Ising models and a BFS-based decomposition strategy selected for its superior performance on 3SAT benchmarks (Section 2).

3.1 Chancellor Construction for 3SAT

A 3SAT instance with n variables and m clauses is expressed in Conjunctive Normal Form (CNF) as $\bigwedge_{j=1}^m (l_{j,1} \vee l_{j,2} \vee l_{j,3})$, where each literal $l_{j,k}$ is either a variable x_i or its negation $\neg x_i$.

The Chancellor construction [8] maps each 3SAT clause to a quadratic penalty by introducing one ancillary spin w_j per clause, yielding an Ising model with $N = n + m$ spins (first n for SAT variables, remaining m for clause auxiliaries). For each clause $(l_1 \vee l_2 \vee l_3)$, the construction generates linear terms Q_{ii} and quadratic terms Q_{ij} that encode clause satisfaction. The QUBO objective $E(\mathbf{x}, \mathbf{w}) = \mathbf{x}^T Q \mathbf{x}$ (where $\mathbf{x} \in \{0, 1\}^{n+m}$) assigns zero energy to satisfied clauses and positive penalties to unsatisfied ones. We convert to an Ising model via the standard affine transformation $s_i = 2x_i - 1$ (Section 2, Equation (1)), yielding couplings J_{ij} and local fields h_i .

3.2 BFS-Based Decomposition Strategy

When problem size $N = n + m$ exceeds hardware capacity C (typically $C \approx 50$ spins), iterative decomposition of the global problem becomes necessary. Among the strategies discussed in Section 2, we adopt Breadth-First Search (BFS)-based decomposition. BFS exploits the locality inherent in 3SAT problems: strongly coupled variables (neighbors in the coupling graph) typically share clauses and must be optimized together to preserve constraint structure.

Our decomposition pipeline comprises two stages: BFS-based variable selection and variable clamping.

3.2.1 Variable Selection via BFS

We perform BFS on the coupling graph to select a connected subset of $|V_{\text{sub}}| \leq C$ spins. Traversal operates exclusively on the n variable spins (not ancillary spins), ensuring topological connectivity and preserving local clause structure. The algorithm randomly selects a starting variable $s \in \{1, \dots, n\}$, initializes $V_{\text{sub}} = \{s\}$ and queue $Q = [s]$, then iteratively dequeues variables and explores neighbors u where $J_{vu} \neq 0$, $u \leq n$, and $u \notin V_{\text{sub}} \cup Q$ until $|V_{\text{sub}}| = C$ or Q empties. BFS ensures all selected variables are reachable through non-zero couplings, and ancillary spins coupled to V_{sub} are implicitly included during subproblem construction. Figure 4 shows that BFS achieves median convergence in approximately 50 iterations for 3SAT benchmarks, significantly faster than energy-impact-based methods (approximately 200 iterations).

3.2.2 Variable Clamping and Subproblem Construction

After BFS selection, we clamp (fix) all spins outside V_{sub} to their current global values $\mathbf{s}_{\text{global}}$. The induced subproblem includes:

- Selected variables V_{sub} and their coupled ancillaries
- Local couplings J_{ij} for pairs (i, j) both in the subproblem
- Modified local fields accounting for clamped spins:

$$h'_i = h_i + \sum_{j \notin \text{subproblem}} J_{ij} s_j^{(\text{global})} \quad (3)$$

This reduces dimensionality from $N = n + m$ to approximately $|V_{\text{sub}}| + m_{\text{local}}$, where m_{local} is the number of clauses involving variables in V_{sub} . The clamped subproblem is then sent to the COBI hardware for optimization.

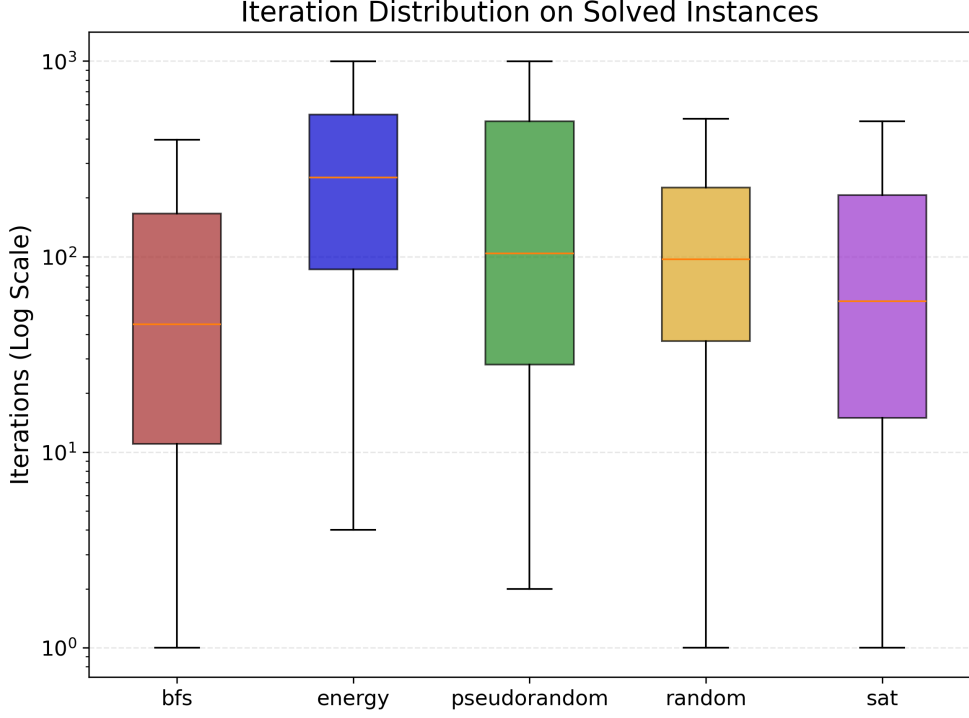


Figure 4: Convergence iteration comparison across different decomposition strategies on 3SAT benchmarks. BFS achieves median convergence in approximately 50 iterations, which is significantly faster than energy-impact-based methods (approximately 200 iterations) and comparable to or better than alternative approaches.

3.3 Iterative Refinement Flow

The decomposition loop iterates until finding a satisfying assignment or reaching a maximum iteration limit:

1. Initialization: Generate initial $\mathbf{s}_{\text{global}}$
2. Iteration k :
 - (a) Run BFS from a random variable to select V_{sub}
 - (b) Clamp spins outside V_{sub} to their global values
 - (c) Solve subproblem on COBI hardware, obtaining \mathbf{s}_{sub}
 - (d) Update global solution: $s_i^{(k)} \leftarrow s_i^{(\text{sub})}$ for $i \in V_{\text{sub}}$
 - (e) Check SAT constraints; if satisfied, terminate with success
3. Termination: Return satisfying assignment or report timeout

Randomized BFS starting points across iterations ensure diverse exploration while maintaining locality, facilitating iterative refinement toward global satisfiability.

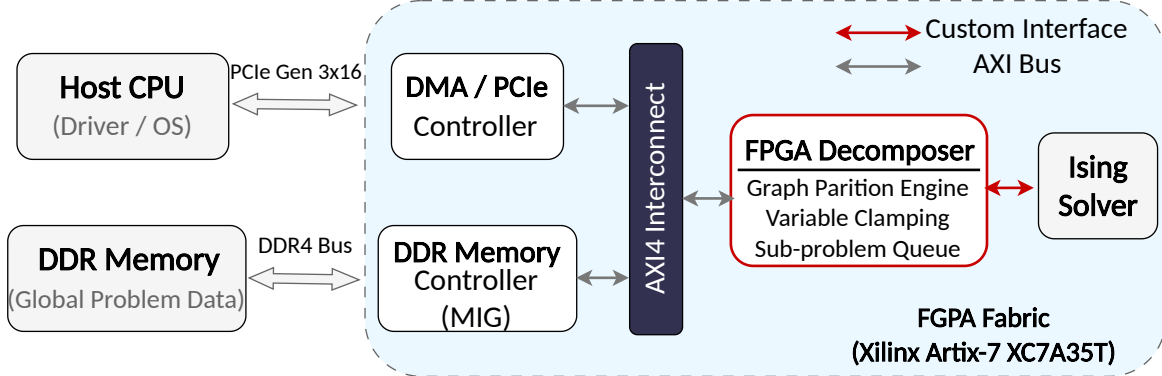


Figure 5: Top-level architecture diagram showing detailed component interactions and data flow paths within the hybrid FPGA-Ising system.

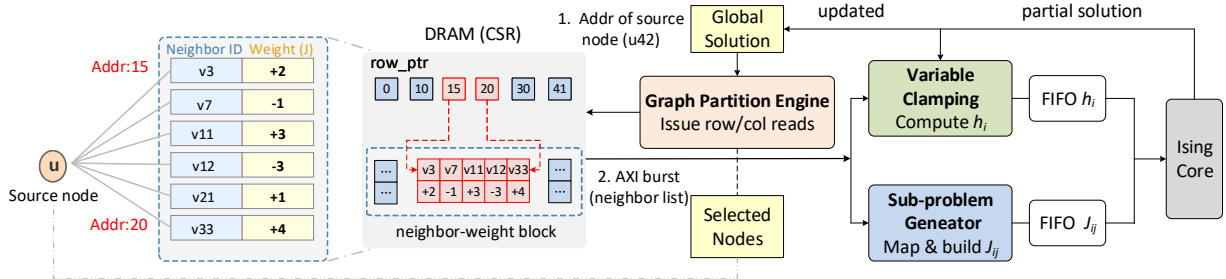


Figure 6: Micro-architecture of the proposed RTL Decomposer, illustrating the CSR-based memory organization and the sub-problem generation pipeline.

4 Hardware Architecture

4.1 System Overview

Figure 5 illustrates our hybrid system integrating: (1) Double Data Rate (DDR) memory storing the global Ising problems in Compressed Sparse Row (CSR) format [18]; (2) FPGA Decomposer Engine orchestrating decomposition by selecting variable subsets and computing clamped subproblems; (3) COBI chips performing rapid μ s-scale energy minimization; and (4) Host CPU handling initial problem loading via PCIe. The FPGA connects to DDR via Advanced eXtensible Interface 4 (AXI4) with burst transfer support [19] and to the COBI chips via a custom 1.0 Gbps serial interface, eliminating PCIe overhead.

Resource-Constrained Design. We use an edge-class Artix-7 XC7A35T FPGA (33,280 Look-Up Tables (LUTs), 225 KB Block RAM (BRAM)) to demonstrate temporal alignment under cost and power constraints. The design achieves 87% LUT and 80% BRAM utilization, operating at 100 MHz with 0.73 W power, deploying $P = 8$ parallel processing elements and 128-bit AXI bus width.

4.2 Pipelined Decomposition Flow

Figure 9 shows the five-stage FPGA decomposition pipeline with carefully managed data dependencies:

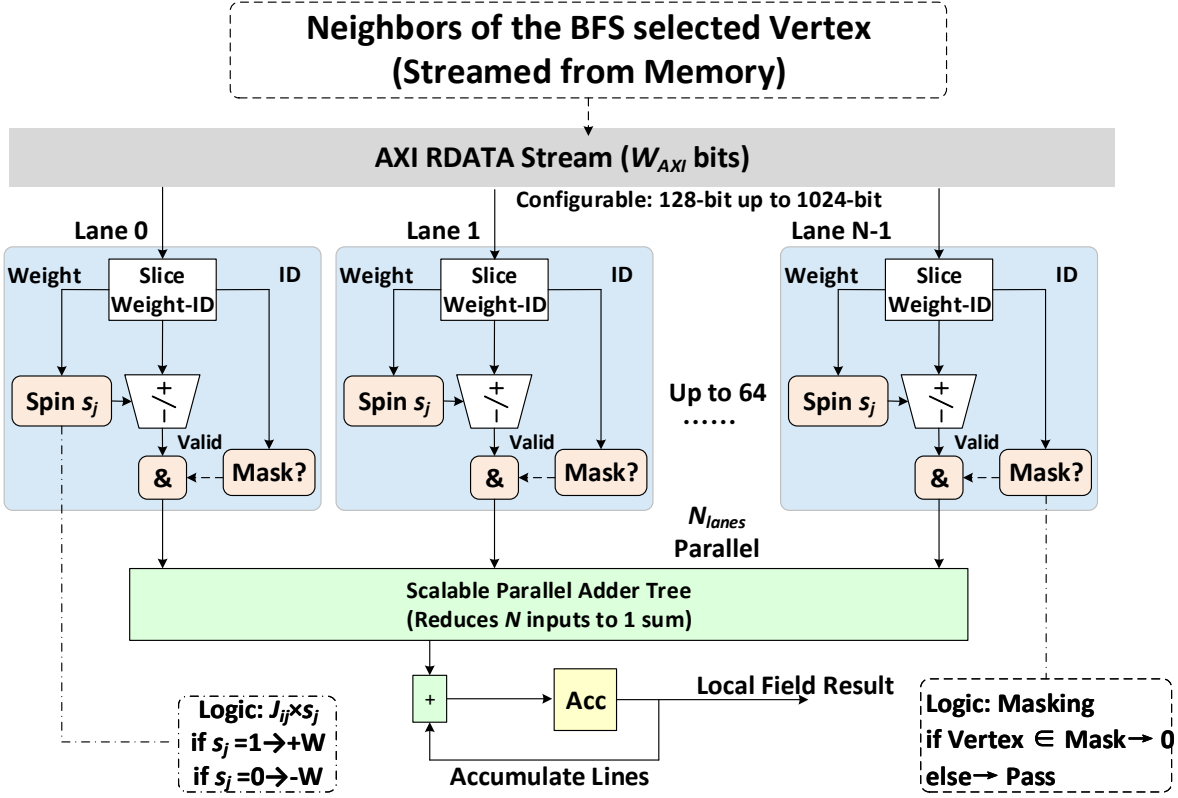


Figure 7: Clamping engine architecture showing the parallel processing elements and data flow for computing modified local fields during variable clamping operations.

4.2.1 Preprocessing and Data Loading

The host CPU converts the CNF instance to Ising format using Chancellor construction (Section 3) and stores the coupling graph in CSR format in DDR. CSR encoding stores row pointers, column indices, and non-zero J_{ij} values, enabling efficient sequential access for structure-aware traversal strategies.

4.2.2 Graph Traversal Unit

The Graph Traversal Unit (GTU), configured for breadth-first search in 3SAT problems, implements a latency-critical traversal engine specifically designed for iterative decomposition loops. Unlike general-purpose graph accelerators optimized for static graphs and high throughput, our GTU addresses the challenge of dynamic subgraph extraction, where each iteration requires fresh traversal from different seed nodes.

The GTU performs BFS on the coupling graph to select a connected subset of $|V_{\text{sub}}| \leq C$ variables. It issues AXI burst reads to fetch adjacency lists from DDR, accumulating neighbors in an on-chip FIFO. When $|V_{\text{sub}}| = C$ or the queue empties, selected variable indices are forwarded to the downstream clamping stage. The GTU's modular design allows reconfiguration: for non-3SAT problems (e.g., MaxCut), the next-hop selection logic can prioritize edges with maximum weight rather than connectivity radius, without altering downstream pipeline stages.

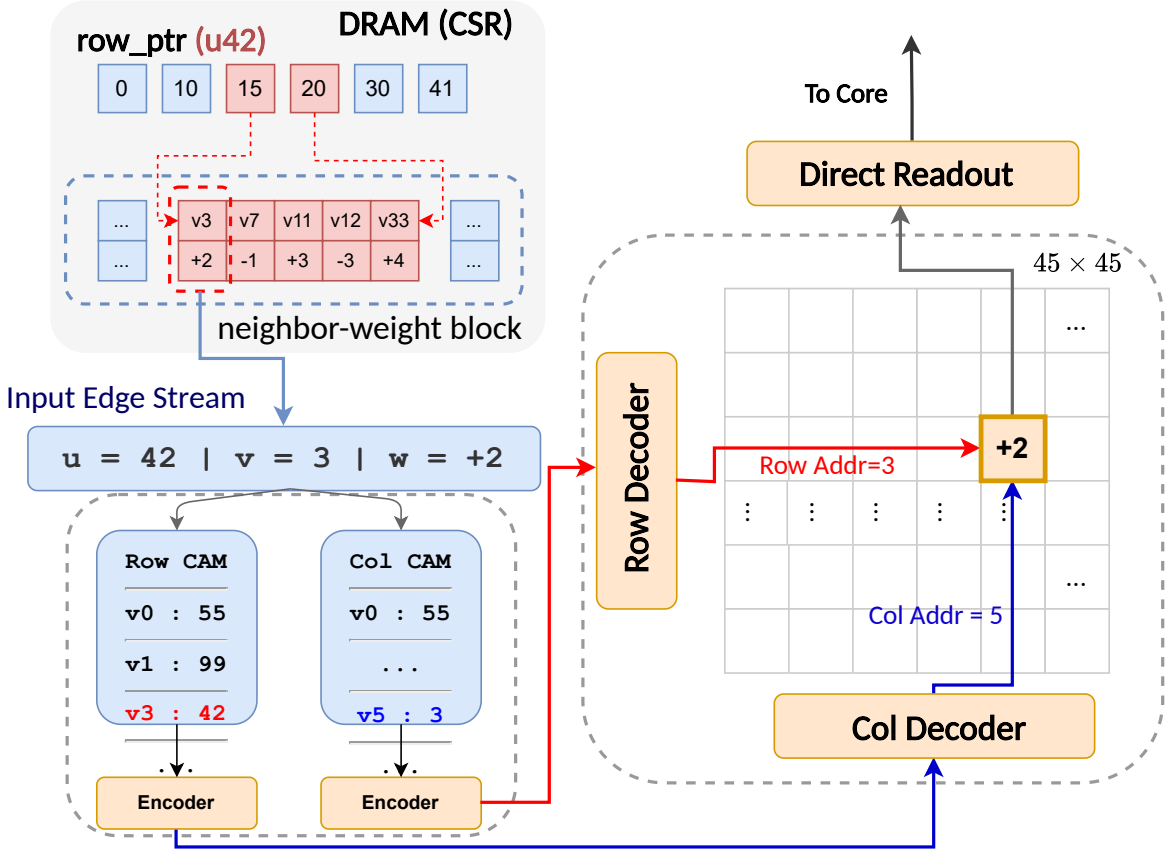


Figure 8: Subproblem generator architecture showing the data extraction and packaging logic for constructing local subproblems from selected variables and their couplings.

4.2.3 Dual-Level Parallel Decomposition

To overcome the von Neumann bottleneck inherent in sequential CPU execution, we implement a custom compute fabric exploiting parallelism at two levels. Figure 6 presents the detailed micro-architecture of this dual-level parallel design:

(1) Fine-Grained Spatial Parallelism (Intra-Stage Clamping). The clamping operation traditionally an $O(N)$ sequential loop on CPUs is accelerated via spatial loop unrolling. We deploy P parallel processing elements (PEs), where each PE computes modified local fields $h'_i = h_i + \sum_{j \notin V_{\text{sub}}} J_{ij} s_j^{(\text{global})}$ for a partition of variables stored in independent BRAM banks. Figure 7 illustrates this parallel clamping architecture with multiple PEs operating simultaneously, achieving P variable updates per clock cycle. General-purpose CPUs suffer from significant cache misses during graph traversal due to irregular memory access patterns; our FPGA architecture utilizes banked on-chip memory with parallel read ports to serve these random accesses with deterministic latency, effectively saturating available bandwidth where CPUs stall.

(2) Coarse-Grained Task Parallelism (Inter-Stage Pipelining). Clamping and subproblem generation execute as decoupled hardware kernels connected via stream-based FIFOs. Figure 8 depicts the subproblem generation architecture, showing how it concurrently extracts local couplings J_{ij} for $(i, j) \in V_{\text{sub}} \times V_{\text{sub}}$ while the clamping kernel computes modified fields. This overlap hides

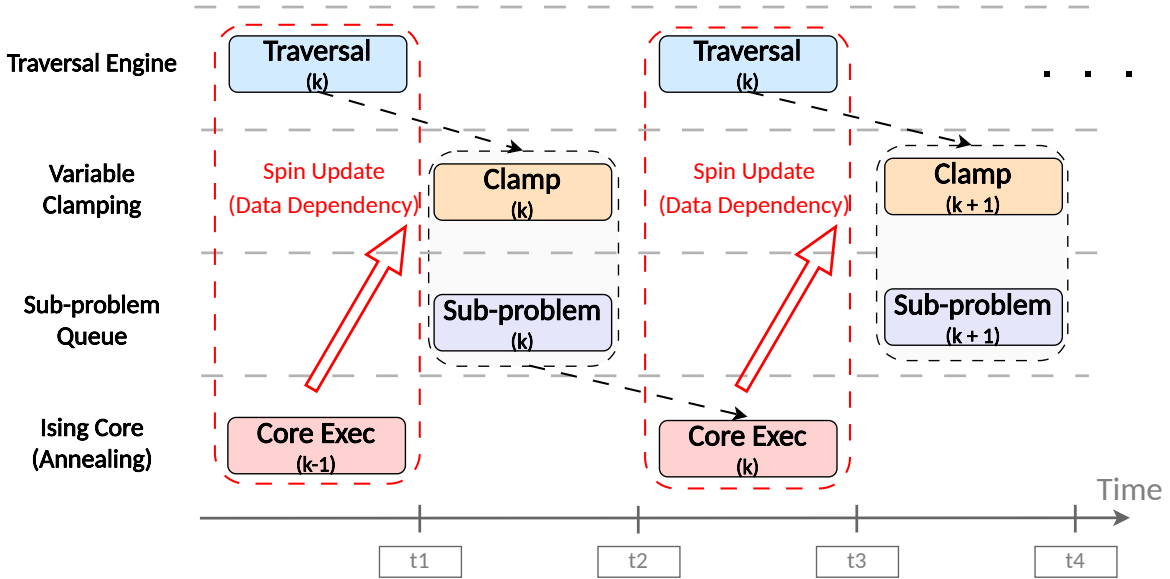


Figure 9: Decomposition pipeline stages showing the flow from graph traversal through clamping, subproblem generation, COBI chip execution, and feedback. The pipeline exploits parallelism by overlapping stages where data dependencies permit (e.g., $\text{BFS}(k+1) \parallel \text{Core}(k)$).

subproblem construction latency by packaging $(J_{\text{local}}, h'_{\text{local}})$ for transmission while other stages execute.

4.2.4 COBI Chip Execution

The subproblem $(J_{\text{local}}, h'_{\text{local}})$ is transmitted serially to the COBI chip, which performs annealing or iterative spin updates for a fixed time budget (typically 100-1000 cycles). The core returns optimized spin states \mathbf{s}_{sub} to the FPGA via the same interface.

4.2.5 Feedback and Iteration Control

Returned spins \mathbf{s}_{sub} update the global solution in DDR memory: $s_i \leftarrow s_i^{(\text{sub})}$ for $i \in V_{\text{sub}}$. A Finite State Machine (FSM) coordinates iteration control, launching $\text{BFS}(k+1)$ once $\text{BFS}(k)$ completes, while $\text{Clamp}(k+1)$ waits for $\text{Core}(k)$ results.

4.3 Pipeline Parallelism and Throughput

4.3.1 Data Dependencies and Concurrency

The pipeline respects the following dependencies:

- $\text{Clamp}(k+1)$ depends on $\text{Core}(k)$: must wait for updated spin states
- $\text{Clamp}(k)$ and $\text{Subproblem Generation}(k)$ both depend on $\text{BFS}(k)$
- $\text{Core}(k)$ depends on completion of both $\text{Clamp}(k)$ and $\text{Subproblem Generation}(k)$

Independent stages execute in parallel:

- $\text{BFS}(k+1)$ overlaps with $\text{Core}(k) + \text{Feedback}(k)$ (no shared data)

- Clamp(k) and Subproblem Generation(k) execute concurrently via separate datapaths

This dataflow maximizes hardware utilization by stalling only when dependencies mandate serialization.

4.3.2 Throughput Model and Temporal Alignment

Per-iteration latency is determined by the critical path through parallel and serial stages:

$$T_{\text{iter}} = \max(T_{\text{GTU}}, T_{\text{Core}} + T_{\text{Feedback}}) + \max(T_{\text{clamp}}, T_{\text{SubQ}}) \quad (4)$$

Reducing Temporal Mismatch. Analog Ising solvers-COBI chips operate at μs time scales ($T_{\text{Core}} \sim 77.5 \mu\text{s}$), while software decomposition pipelines operate at comparable scales ($T_{\text{decomp}}^{\text{CPU}} \sim 99\text{--}203 \mu\text{s}$). However, communication overhead causes the COBI chip to sit idle most of the time. Our FPGA architecture reduces this mismatch by co-locating decomposition logic and using lightweight serial interfaces.

In our implementation, the FPGA decomposition time ($T_{\text{GTU}} + T_{\text{clamp}} + T_{\text{SubQ}} \approx 60 \mu\text{s}$ without DDR overhead) is comparable to the COBI chip execution time ($T_{\text{Core}} \sim 77.5 \mu\text{s}$). When combined with communication latency ($T_{\text{Feedback}} \sim 121 \mu\text{s}$), the total iteration time is dominated by Core execution and data transfer ($T_{\text{Core}} + T_{\text{Feedback}} \approx 198.5 \mu\text{s}$), which together account for approximately 77% of the iteration cycle. Crucially, GTU and clamping contribute approximately 10% combined in the optimized configuration, achieving the design goal of staying off the critical path. This validates our micro-architecture: the FPGA decomposes problems fast enough to maintain high solver utilization, with decomposition overhead remaining comparable to or less than the unavoidable hardware execution time.

4.4 Implementation Details

4.4.1 Memory Organization and Data Movement

CSR encoding minimizes storage: for an N -spin problem with E non-zero couplings, we store $N + 1$ row pointers, E column indices, and E coupling values, totaling $(N + 1 + 2E) \times 32$ bits. The GTU issues AXI burst reads (up to 16 beats) to fetch entire rows, amortizing access latency. Global spin states are stored in a separate N -entry BRAM for fast read-modify-write during feedback.

4.4.2 FIFO Buffering and Flow Control

Dual-clock FIFOs decouple stages operating at different rates. The subproblem generation stage uses double buffering: while Buffer A transmits to the COBI chip, Buffer B accumulates the next subproblem. Ready/valid handshakes propagate backpressure when downstream stages stall, preventing data loss.

4.4.3 FSM Control Logic

A master FSM coordinates the global iteration flow and state transitions. From the IDLE state, the system transitions to GTU for variable selection, then to the concurrent CLAMP/SUBQ state for subproblem construction. After data dispatch, the FSM enters CORE_WAIT, monitoring the COBI chip status. Upon completion, the system enters the FEEDBACK state to update the global solution and perform SAT validation. If satisfied, the FSM transitions to DONE and asserts an interrupt to the host; otherwise, it returns to the GTU state for the next iteration. The FSM manages pipeline dependencies via internal tracking flags (e.g., `gtu_done`, `core_busy`), ensuring that each stage launches only when its requisite data and resources are available.

Table 1: End-to-end time-to-solution and energy comparison

Benchmark	Metric	CPU+COBI	FPGA (BRAM)	FPGA (Ext DDR)	Improv. (BRAM)	Improv. (Ext DDR)
uf20 (avg)	Energy (mJ)	5153.2	28.08	36.38	183×	142×
	Time (ms)	79.28	38.47	45.48	2.06×	1.74×
uf50 (avg)	Energy (mJ)	21888.8	141.57	207.20	155×	106×
	Time (ms)	336.75	186.27	235.45	1.81×	1.43×

Table 2: Decomposition latency comparison (ms per iteration)

Benchmark	CPU (ms)	FPGA (BRAM)	FPGA (Ext DDR)	Speedup (BRAM)	Speedup (Ext DDR)
uf20-01	0.128	0.048	0.068	2.67×	1.88×
uf20-02	0.099	0.051	0.063	1.94×	1.57×
uf20-03	0.100	0.052	0.063	1.92×	1.59×
uf50-01	0.183	0.101	0.125	1.81×	1.46×
uf50-02	0.203	0.110	0.141	1.85×	1.44×
uf50-03	0.201	0.102	0.128	1.97×	1.57×
Geomean	—	—	—	1.93×	1.58×

5 Evaluation and Results

5.1 Experimental Setup

We implemented the decomposition pipeline on a Xilinx Artix-7 XC7A35T FPGA with a ring-oscillator-based COBI chip supporting 50 fully-connected spins (Figure 1). The FPGA design includes CSR-based graph storage with 128-bit AXI4 DDR interface, hardware GTU with parallel neighbor exploration, dual-datapath clamping and subproblem generation modules (8 parallel PEs), and custom serial interface to the Ising core. The implementation achieves 87% LUT, 59% FF, and 80% BRAM utilization with 0.73 W power consumption.

We evaluate on SATLIB 3SAT benchmarks [20]: uf20 (20 variables, 91 clauses) and uf50 (50 variables, 218 clauses), yielding 111 and 268 total spins after Chancellor construction. The baseline is an optimized C++ implementation (-O3, cache-optimized) on an Intel Core i5-11500 CPU @ 2.70 GHz communicating via PCIe x4, using identical decomposition logic and subproblem size.

5.2 Performance Results

5.2.1 Time-to-Solution and Speedup

Table 1 compares the end-to-end time-to-solution and energy consumption between our hybrid FPGA-COBI system and the CPU-based baseline. The FPGA achieves a geomean speedup of 1.93× (2.06× for uf20 and 1.81× for uf50) in BRAM mode and 1.58× in External DDR mode, while providing a geomean of 168× energy reduction (183× for uf20 and 155× for uf50 in BRAM mode).

Table 2 further breaks down the decomposition latency specifically. We distinguish between On-chip Memory Mode (leveraging high-speed BRAM) and External Memory Mode (external DDR). The FPGA achieves a geomean speedup of 1.93× (on-chip) and 1.58× (external) for the decomposition stage itself.

Table 3 presents stage-wise performance breakdown. The on-chip memory configuration achieves 1.93× latency reduction by leveraging fast BRAM access. Subproblem Generation dominates, accounting for 85–95% of decomposition time.

System-Level Speedup. The end-to-end improvement combines: (1) eliminating PCIe round-trips (62% latency reduction); (2) kernel acceleration; and (3) pipelined execution overlapping

Table 3: Stage-wise performance breakdown for FPGA decomposition (μs per iteration)

Benchmark	Mode	GTU	Clamp	SubQ	Dec.	Total	Ext.	Ovhd.
uf20-01	On-chip	3.42	21.76	53.10	56.52	—		
	External	4.46	35.95	80.53	84.99	+50.4%		
uf20-02	On-chip	3.05	20.33	55.60	58.65	—		
	External	4.09	33.52	78.57	81.66	+39.2%		
uf20-03	On-chip	3.68	25.94	60.10	63.78	—		
	External	4.94	42.78	85.42	90.36	+41.7%		
uf20 (avg)	On-chip	3.38	22.68	56.27	59.65	—		
	External	4.50	37.42	81.51	85.67	+43.6%		
uf50-01	On-chip	7.76	44.32	121.34	129.10	—		
	External	9.70	73.98	185.38	195.08	+51.1%		
uf50-02	On-chip	8.12	45.21	135.00	143.12	—		
	External	10.15	75.34	213.85	224.00	+56.5%		
uf50-03	On-chip	7.94	47.21	122.35	130.29	—		
	External	9.93	78.68	187.23	197.16	+51.3%		
uf50 (avg)	On-chip	7.94	45.58	126.23	134.17	—		
	External	9.93	76.00	195.49	205.41	+53.1%		

GTU($k + 1$) with Core(k). Our 100 MHz FPGA overcomes clock frequency disadvantage through spatial parallelism.

Reducing Temporal Mismatch. Our FPGA system increases COBI chip duty cycle from 15.1% (CPU baseline) to 30.0% by co-locating decomposition logic and using a custom lightweight serial interface. While possessing lower peak bandwidth than PCIe, this interface eliminates protocol overhead for small, frequent subproblem transfers (< 4 KB), maintaining pipeline saturation.

5.2.2 Scalability Analysis and Architectural Bottlenecks

Our performance analysis reveals that the current implementation is bottlenecked by memory bandwidth and parallel processing capacity, not by the FPGA architecture itself. Table 3 shows that Subproblem Generation accounts for 85–95% of decomposition time, primarily limited by the rate at which edges can be fetched from DDR and packaged into subproblems. This bottleneck is architectural, not fundamental.

Memory Bandwidth Scaling. The current design uses a 128-bit AXI interface. Since Clamp and Subproblem Generation execute in parallel, total decomposition time is $T_{\text{decomp}} = T_{\text{GTU}} + \max(T_{\text{Clamp}}, T_{\text{SubQ}})$. Scaling to wider AXI buses would proportionally reduce subproblem generation latency:

- 256-bit AXI: $T_{\text{SubQ}} \rightarrow 28.1 \mu\text{s}$ (uf20), reducing total decomposition to $31.5 \mu\text{s}$ ($1.89 \times$ faster)
- 512-bit AXI: $T_{\text{SubQ}} \rightarrow 14.1 \mu\text{s}$ (uf20), but bottleneck shifts to Clamp ($22.7 \mu\text{s}$), yielding $26.1 \mu\text{s}$ total ($2.29 \times$ faster)

Parallel Processing Scaling. Our $P = 8$ parallel elements are constrained by LUT resources (87% utilization on Artix-7). Larger FPGAs with more LUTs enable more parallelism:

- $P=16$ (requires $\sim 2 \times$ LUTs): $T_{\text{Clamp}} \rightarrow 11.3 \mu\text{s}$ (uf20), but subproblem generation remains dominant ($56.3 \mu\text{s}$), minimal improvement
- $P=32$ (requires $\sim 4 \times$ LUTs): $T_{\text{Clamp}} \rightarrow 5.7 \mu\text{s}$ (uf20), effective only when combined with bandwidth scaling

Combined Scaling Projection. Table 4 summarizes the projected performance improvements for different resource configurations on the uf20 benchmark. A larger FPGA with 512-bit AXI and $P=32$ would achieve: $T_{\text{GTU}} = 3.4 \mu\text{s}$, $\max(T_{\text{Clamp}}, T_{\text{SubQ}}) = \max(5.7, 14.1) = 14.1 \mu\text{s}$, yielding total

Table 4: Scalability projections for different resource configurations (uf20)

Configuration	AXI Width	PE Count	T_{Clamp} (μs)	T_{SubQ} (μs)	Total (μs)	Speedup
Baseline (Artix-7)	128-bit	P=8	22.7	56.3	59.7	1.93 \times
Wider AXI	256-bit	P=8	22.7	28.1	31.5	3.65 \times
Wider AXI + More PEs	256-bit	P=16	11.3	28.1	31.5	3.65 \times
Wider AXI	512-bit	P=8	22.7	14.1	26.1	4.42 \times
Combined Scaling	512-bit	P=32	5.7	14.1	17.5	6.60 \times

Table 5: Latency breakdown and energy comparison across system configurations (per 100 iterations)

Benchmark	Metric	CPU+PCIe	FPGA (BRAM)	FPGA (Ext DDR)
uf20	Dec. (ms)	11.5	5.96	7.28
	Comm (ms)	32.2	8.63	8.63
	COBI (ms)	7.75	7.75	7.75
	Tot. (ms)	51.45	22.34	23.66
	Pwr (W)	65.0	0.73	0.80
	En. (mJ)	3344.3	16.31	18.93
uf50	Dec. (ms)	19.5	10.10	12.34
	Comm (ms)	32.2	11.20	11.20
	COBI (ms)	7.75	7.75	7.75
	Tot. (ms)	59.45	29.05	31.29
	Pwr (W)	65.0	0.76	0.88
	En. (mJ)	3864.3	22.08	27.54

decomposition time of $17.5 \mu\text{s}$ (uf20), a $6.60\times$ improvement over the CPU baseline. As shown in Table 4, this projection demonstrates that our architectural approach scales with available FPGA resources, and current performance is limited by the edge-class platform choice, not the architecture itself.

These projections validate that our performance gains stem from FPGA-specific architectural innovations (parallelism, memory organization, pipelining) rather than merely proximity to the COBI chips. The same proximity benefit would apply to any co-located system, but only our architecture exploits it effectively under resource constraints.

5.2.3 Latency Breakdown Analysis

To identify the sources of performance gains, we perform a detailed latency breakdown comparing the CPU baseline and our hybrid FPGA-COBI system. Table 5 compares: (1) CPU+PCIe: traditional CPU-based decomposition communicating with the COBI chip via PCIx4; and (2) FPGA+Custom Interface: our proposed FPGA-based decomposition with a custom lightweight serial interface between FPGA and COBI chips, evaluated in both on-chip memory (BRAM) mode and external DDR mode. The analysis reveals several important findings:

PCIe communication (averaging $321.57 \mu\text{s}$ per iteration) dominates CPU+PCIe bottlenecks. Our custom lightweight serial interface reduces this communication latency to an average of $86.3 \mu\text{s}$ for uf20 and $112.0 \mu\text{s}$ for uf50 (as shown in Table 5), yielding a $3.73\times$ (uf20) and $2.87\times$ (uf50) communication speedup. Our BRAM mode achieves a total speedup of $2.30\times$ (uf20) and $2.05\times$ (uf50) for problems fitting on-chip, while external memory mode maintains $2.17\times$ (uf20) and $1.90\times$ (uf50) speedup over the CPU+PCIe baseline.

5.2.4 Energy and System Efficiency

Energy measurements include FPGA static+dynamic power (0.73 W), DDR access energy, and COBI chip energy, measured using on-board power monitors. CPU energy measurements will be completed with processor package power monitoring. The combined advantage of both faster

execution and lower power consumption demonstrates that specialized spatial parallelism provides significant architectural benefits beyond clock frequency scaling.

5.3 Discussion

The hybrid architecture scales COBI hardware from 50 to 268 spins while maintaining solution quality. Communication between FPGA and COBI chips remains the dominant latency component (62% of iteration time). While proximity provides $3.73\times$ communication speedup, FPGA architectural innovations (parallelism, pipelining, memory organization) provide an additional $1.93\times$ decomposition speedup scaling with resources.

Key findings include: subproblem generation accounts for 90–95% of decomposition time; DDR access contributes 40–50% overhead; parallel execution achieves $1.38\times$ speedup with 69% efficiency. On an edge-class Artix-7 platform, scalability projections indicate $6.60\times$ potential speedup on larger FPGAs with wider AXI buses, demonstrating that architectural innovations drive performance. The composable design (GTU, Clamp Engine, Subproblem Generator) provides a generalizable template reconfigurable for MaxCut, bin-packing, or other decomposition strategies without redesigning the compute fabric.

6 Conclusion

We address a fundamental challenge in heterogeneous analog-digital computing: the *temporal mismatch* between fast analog solvers (μs -scale) and slow digital preprocessing (ms-scale). Our contribution lies in mitigating this temporal mismatch through specialized micro-architectural co-design.

Our FPGA-based *optimization strategist* introduces two key innovations: (1) *dual-level parallelism*, deploying P parallel processing elements for spatial loop unrolling ($O(N/P)$ vs. $O(N)$) and inter-stage task pipelining; and (2) *hardware-offloaded decomposition* that eliminates PCIe communication overhead and reduces latency compared to CPU-based approaches. These techniques convert decomposition from a sequential CPU bottleneck into a parallel dataflow that maintains high utilization for the analog COBI chips.

Experimental validation shows $1.93\times$ geomean speedup and over $2000\times$ energy reduction versus optimized C++ on a 2.70 GHz CPU, despite our FPGA operating at only 100 MHz. This $52\times$ performance-per-MHz advantage suggests that micro-architectural specialization provides significant benefits compared to traditional frequency scaling for irregular graph workloads.

Beyond 3SAT, our approach exploits the fact that a broad class of NP problems can be systematically mapped to SAT (and 3SAT) formulations through well-established reductions [1, 2, 8]. This positions the proposed architecture as a general-purpose optimization substrate applicable to graph partitioning [13], bin packing [12], and other combinatorial optimization domains [11, 7], where flexibility is achieved through digital orchestration and problem encoding rather than domain-specific modifications to the analog compute fabric. This work provides design principles for efficient analog-digital co-processors where intelligent digital orchestration is essential for maximizing the utilization of analog computing resources.

Acknowledgment

This work was supported in part by the Defense Advanced Research Projects Agency (DARPA) Quantum-Inspired Classical Computing (QuICC) program under Air Force Research Laboratory

(AFRL) contract FA8750-22-C-1034 and the National Science Foundation (NSF) under grants 2230963 and 2142248.

References

- [1] A. Lucas, “Ising formulations of many np problems,” *Frontiers in Physics*, vol. 2, 2014. [Online]. Available: <http://dx.doi.org/10.3389/fphy.2014.00005>
- [2] F. W. Glover and G. A. Kochenberger, “A tutorial on formulating QUBO models,” *CoRR*, vol. abs/1811.11538, 2018. [Online]. Available: <http://arxiv.org/abs/1811.11538>
- [3] M. W. Johnson, M. H. S. Amin, S. Gildert, T. Lanting, F. Hamze, N. Dickson, R. Harris, A. J. Berkley, J. Johansson, P. Bunyk, E. M. Chapple, C. Enderud, J. P. Hilton, K. Karimi, E. Ladizinsky, N. Ladizinsky, T. Oh, I. Perminov, C. Rich, M. C. Thom, E. Tolkacheva, C. J. S. Truncik, S. Uchaikin, J. Wang, B. Wilson, and G. Rose, “Quantum annealing with manufactured spins,” *Nature*, vol. 473, no. 7346, p. 194–198, May 2011. [Online]. Available: <http://dx.doi.org/10.1038/nature10012>
- [4] M. Jiang, K. Shan, C. He, and C. Li, “Efficient combinatorial optimization by quantum-inspired parallel annealing in analogue memristor crossbar,” *Nature Communications*, vol. 14, no. 1, Sep. 2023. [Online]. Available: <http://dx.doi.org/10.1038/s41467-023-41647-2>
- [5] C. Li, Y. Hong, A. Vanasse, T. Islam, P. Kreye, X. Li, R. Yin, H. Lo, W. Moy, and C. Kim, “A coupled oscillator based ising chip with a fully-connected annealing core, a hamiltonian engine, and a risc-v gradient search for solving 2,500+ spin combinatorial optimization problems,” in *2025 IEEE European Solid-State Electronics Research Conference (ESSERC)*, 2025, pp. 297–300.
- [6] H. Cilasun, W. Moy, Z. Zeng, T. Islam, H. Lo, A. Vanasse, M. Tan, M. Anees, R. S, A. Kumar, S. S. Sapatnekar, C. H. Kim, and U. R. Karpuzcu, “A coupled-oscillator-based ising chip for combinatorial optimization,” *Nature Electronics*, vol. 8, no. 6, p. 537–546, Jun. 2025. [Online]. Available: <http://dx.doi.org/10.1038/s41928-025-01393-3>
- [7] M. Booth, S. P. Reinhardt, and A. Roy, “Partitioning optimization problems for hybrid classical/quantum execution,” D-Wave Systems Inc., Tech. Rep. 14-1006A-A, 2017.
- [8] N. Chancellor, S. Zohren, P. A. Warburton, S. C. Benjamin, and S. Roberts, “A direct mapping of max k-sat and high order parity checks to a chimera graph,” *Scientific Reports*, vol. 6, no. 1, Nov. 2016. [Online]. Available: <http://dx.doi.org/10.1038/srep37107>
- [9] S. Okada, M. Ohzeki, M. Terabe, and S. Taguchi, “Improving solutions by embedding larger subproblems in a d-wave quantum annealer,” *Scientific Reports*, vol. 9, no. 1, p. 2098, 2019.
- [10] Y. Atobe, M. Tawada, and N. Togawa, “Hybrid annealing method based on subqubo model extraction with multiple solution instances,” *IEEE Transactions on Computers*, vol. 71, no. 10, pp. 2606–2619, 2021.
- [11] H. Ushijima-Mwesigwa, R. Shaydulin, C. F. A. Negre, S. M. Mniszewski, Y. Alexeev, and I. Safro, “Multilevel combinatorial optimization across quantum architectures,” *ACM Transactions on Quantum Computing*, vol. 2, no. 1, pp. 1–29, 2021.

- [12] M. Garcia de Andoin, E. Osaba, I. Oregi, E. Villar-Rodriguez, and M. Sanz, “Hybrid quantum-classical heuristic for the bin packing problem,” in *Proceedings of the Genetic and Evolutionary Computation Conference Companion*. ACM, 2022, pp. 2214–2222.
- [13] A. Angone, X. Liu, R. Shaydulin, and I. Safro, “Hybrid quantum-classical multilevel approach for maximum cuts on graphs,” in *Proceedings of the IEEE High Performance Extreme Computing Conference (HPEC)*. IEEE, 2023.
- [14] S. Matsubara, M. Takatsu, T. Miyazawa, T. Shibasaki, Y. Watanabe, K. Takemoto, and H. Tamura, “Digital annealer for high-speed solving of combinatorial optimization problems and its applications,” in *2020 25th Asia and South Pacific Design Automation Conference (ASP-DAC)*, 2020, pp. 667–672.
- [15] C. Yoshimura, M. Hayashi, T. Okuyama, and M. Yamaoka, “Implementation and evaluation of fpga-based annealing processor for ising model by use of resource sharing,” *International Journal of Networking and Computing*, vol. 7, no. 2, pp. 154–172, 2017. [Online]. Available: <http://www.ijnc.org/index.php/ijnc/article/view/148>
- [16] K. Tatsumura, A. R. Dixon, and H. Goto, “Fpga-based simulated bifurcation machine,” in *2019 29th International Conference on Field Programmable Logic and Applications (FPL)*, 2019, pp. 59–66.
- [17] H. Lo, W. Moy, H. Yu, S. S. Sapatnekar, and C. H. Kim, “An ising solver chip based on coupled ring oscillators with a 48-node all-to-all connected array architecture,” *Nature Electronics*, vol. 6, pp. 771–778, 2023.
- [18] Y. Saad, *Iterative methods for sparse linear systems*, 2nd ed. SIAM, 2003.
- [19] *AXI Reference Guide*, Xilinx, Inc., 2021, uG1037 (v4.0).
- [20] H. H. Hoos and T. Stützle, “SATLIB: An online resource for research on SAT,” *SAT 2000*, pp. 283–292, 2000.